

## Article

# In-Situ Grown Nanohydroxyapatite on Graphene Oxide Nanoscrolls for Modulated Physicochemical Properties of Poly (Caprolactone) Composites

Lillian Tsitsi Mambiri, Gabrielle Broussard, Ja' Caleb Smith and Dilip Depan \* 

Chemical Engineering Department, Institute for Materials Research and Innovation, University of Louisiana at Lafayette, P.O. Box 44130, Lafayette, LA 70504-4130, USA

\* Correspondence: ddepan@louisiana.edu; Tel.: +1-337-654-0943

**Abstract:** Polymer composites with exceptional bioactivity and controlled in vitro degradation are crucial in tissue engineering. A promising approach involves combining graphene oxide nanoscrolls (GONSs) and nanohydroxyapatite (nHA) with polycaprolactone (PCL). The synergy of these components enables the mineralization of nHA within GONSs through a two-step process: first, oxygen-containing anionic groups in the GONSs anchor  $\text{Ca}^{2+}$  ions, followed by the formation of dispersed nHA through chelation with  $\text{CaHPO}_4^{2-}$  via electrovalent bonding. A thermal analysis of the scaffolds' morphology and microstructure was conducted via DSC and SEM imaging. Its enhanced physical properties are attributed to interactions between PCL and nHA–GONSs, as confirmed by an FTIR analysis showing strong interfacial bonding. Enzymatic degradation studies demonstrated reduced weight loss in PCL–nHA–GONS composites over 21 days, highlighting GONSs' role in enhancing dimensional stability and reinforcement. An EDS analysis post-degradation revealed increased  $\text{Ca}^{2+}$  deposition on scaffolds with nHA–GONSs, indicating improved biopolymer–bioceramic interaction facilitated by the GONSs' scrolled structure. This research offers a straightforward yet effective method for functionalizing GONSs with biologically beneficial nHA, potentially advancing graphene-based biomaterial development.

**Keywords:** polycaprolactone; nanohydroxyapatite; graphene oxide nanoscrolls; biomineralization



**Citation:** Mambiri, L.T.; Broussard, G.; Smith, J.; Depan, D. In-Situ Grown Nanohydroxyapatite on Graphene Oxide Nanoscrolls for Modulated Physicochemical Properties of Poly (Caprolactone) Composites.

*Macromol* **2024**, *4*, 285–303. <https://doi.org/10.3390/macromol4020017>

Academic Editor: Denis Mihaela Panaitescu

Received: 8 April 2024

Revised: 4 May 2024

Accepted: 8 May 2024

Published: 11 May 2024



**Copyright:** © 2024 by the authors. Licensee MDPI, Basel, Switzerland. This article is an open access article distributed under the terms and conditions of the Creative Commons Attribution (CC BY) license (<https://creativecommons.org/licenses/by/4.0/>).

## 1. Introduction

Annually, tens of millions of patients grapple with bone defects, necessitating a pressing global requirement for implants and biomaterials dedicated to bone defect repair [1]. Polymeric biomaterials and composites are highly sought after for tissue engineering applications because they can be customized and tailored for specific properties. Synthetic polymers such as polycaprolactone (PCL), poly (lactic-co-glycolic acid) (PLGA), polylactic acid (PLA), and polyurethane (PU) are favored for their biocompatibility, biodegradability, and mechanical strength [2–4]. PCL is desirable for tissue engineering scaffolds due to its biocompatibility, ensuring no adverse reactions when introduced to the body [5]. PCL balances strength and flexibility, mimicking various physical tissue properties. Its low melting point enables easy processing for fabrication methods [5]. However, its limitations include a deficiency in bioactivity [6]. Despite being hydrophobic, PCL can permit the controlled absorption and release of bioactive molecules through functionalization, enhancing tissue regeneration [7]. Many composite scaffolds have been effectively created by integrating synthetic biopolymers with inorganic bioactive fillers like hydroxyapatite (HA) [8,9].

Bioceramics like HA whiskers are extensively researched for bone regeneration due to their osteogenic potential. However, their brittle nature limits their use. To address this, bioceramics are being developed in nano- and microshapes, such as nanohydroxyapatite (nHA), which can enhance their mechanical properties [10]. They are commonly used as reinforcement fillers because their composition is similar to that of calcified tissues,

providing bioactivity [11]. nHA bone mineral is beneficial in tissue engineering scaffolds as it promotes bone regeneration, encourages osteoblast adhesion, proliferation, and differentiation, and can bind to bone tissue and facilitate bone healing when used in orthopedic and dental applications [12–14]. PCL–nHA scaffolds are also considered affordable due to their low production costs and effective, scalable manufacturing methods [15]. Nevertheless, the mechanical properties of nHA, such as its stiffness and brittleness, have hindered its widespread use [16]. In addition to mechanical stability, a series of pressing challenges persistently demand resolution, explicitly about dispersion efficacy and interface compatibility [16]. These limitations can be effectively overcome by combining nHA with mechanically reinforced materials like graphene oxide (GO).

In recent years, carbon nanomaterials, particularly GO and its derivatives, have gained significant attention due to their unique properties and wide range of applications [16,17]. GO is composed of hydrophilic single-layer nanosheets due to hydroxyl, carboxyl, and epoxy groups [7]. However, GO has certain drawbacks, including the tendency for its sheets to agglomerate or overlap [18]. Agglomeration reduces the active surface area and limits its potential applications in adsorption, drug delivery, and filtration membranes [18]. Nonetheless, GO's flat and thin structure offers the flexibility to make structural and morphological modifications, which is a promising solution to overcome these disadvantages [7,19]. The oxygen functional groups located at the edges of GO sheets serve as both functional sites and spacers, facilitating the conversion of GO into various nanomorphologies through structural and functional adjustments [17].

Graphene oxide nanoscrolls (GONSs) potentially outperform other GO derivatives due to their scrolled structure [18]. GONSs can be easily fabricated by rolling graphene oxide sheets with different sizes and functionalizations, which can modulate the nanoscrolls' diameter, surface charge, and chemical reactivity [16,18,20]. Their large surface area, derived from the scrolled structure, allows for stronger interfacial bonding in a matrix, resulting in improved mechanical properties owing to low agglomeration in porous structures [18].

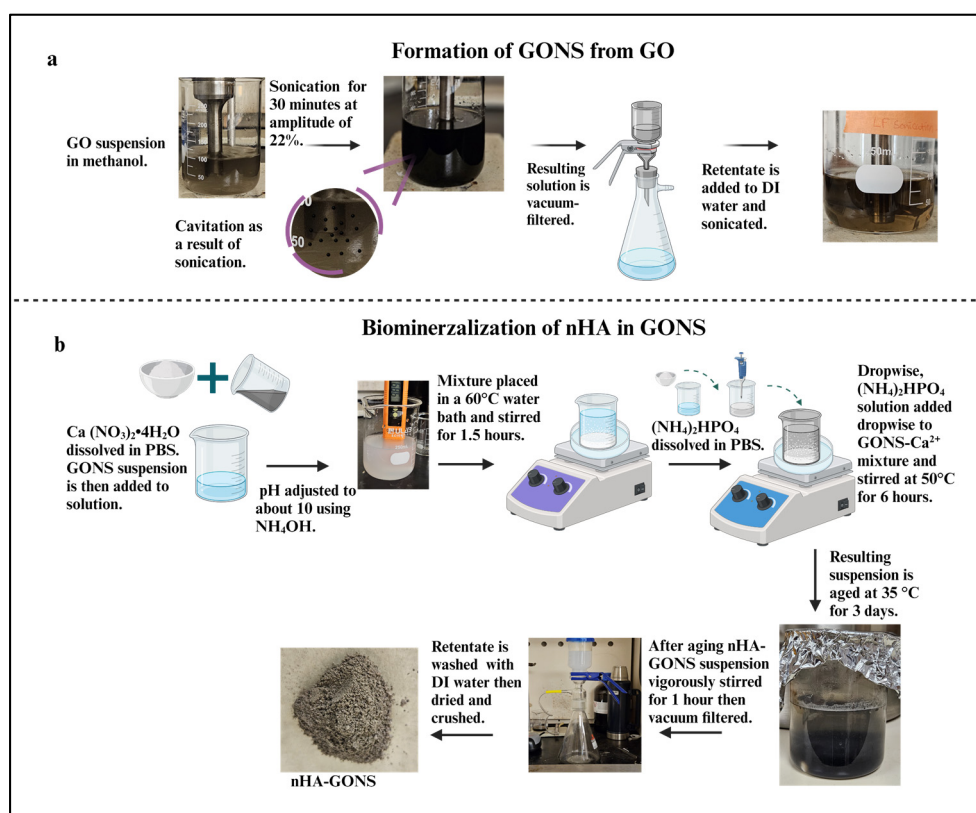
The main objectives of this novel study are to fabricate and characterize PCL–nHA–GONS composites. The primary focus is modulating the composites' physical properties and evaluating their *in vitro* degradation. The key attributes of our approach are (1) a low GONS concentration, not only to provide functional groups to nucleate or mineralize nHA but also to facilitate uniform dispersion in the PCL matrix, and (2) mild experimental conditions (pH 7.4 and room temperature) to control the size and morphology of nHA crystals. The integration of GONSs represents a groundbreaking innovation, offering an unparalleled advantage compared to other nanofillers. This unique approach aims to enhance interfacial bonding and significantly elevate biomineralization and mechanical properties within the composite. The scrolled morphology of GONSs offers an expansive surface area, providing numerous nucleation sites for the formation and growth of nHA. These sites are critical for promoting the deposition of calcium phosphate nanocrystals. Additionally, GONSs are rich in reactive functional groups such as carboxyl, hydroxyl, and epoxy groups, which interact electrostatically and chemically with calcium and phosphate ions. This interaction not only aids in the initial binding and localization of these crucial ions but also in their sustained retention and controlled release. This controlled release mechanism ensures a continuous supply of the necessary minerals, facilitating a gradual and sustained biomineralization process essential for effective bone regeneration. Furthermore, the resulting enhanced interfacial bonding leads to superior mechanical properties, ensuring heightened structural integrity and stability for the biomaterial. Significantly, the ease of fabrication and the affordability of GONSs add an additional advantage, making this pioneering application technically superior and accessible for widespread use. These insights have the potential to redefine the biomaterial landscape, making it exceptionally well suited for diverse applications in bone regeneration and other biomedical fields.

## 2. Materials and Methods

Graphene oxide (GO) aqueous dispersion (5 mg/mL) was obtained from Goographene, Merrifield, VA, USA. Methanol was acquired from Carolina Biological Supply Company, Burlington, North Carolina, USA. PCL (average Mn 80,000), calcium nitrate tetrahydrate ( $\text{Ca}(\text{NO}_3)_2 \cdot 4\text{H}_2\text{O}$ ), lysozyme, dichloromethane (DCM), and diammonium phosphate ( $(\text{NH}_4)_2\text{HPO}_4$ ) were purchased from Sigma-Aldrich, Milwaukee, WI, USA. Ammonium hydroxide ( $\text{NH}_4\text{OH}$ ) was purchased from EMD Millipore Corporation, Burlington, MA, USA. Phosphate buffer saline (PBS) was purchased from Fisher Scientific, Waltham, MA, USA.

### 2.1. Nanofiller Preparation

The GONSs were prepared using a low-frequency (LF) ultrasonication technique (Scheme 1a) [18]. Meanwhile, the nHA and nHA–GONSs were prepared via a wet chemical technique (Scheme 1b) [21].



**Scheme 1.** (a) Schematic diagram detailing the preparation of graphene oxide nanoscrolls through low-frequency ultrasonication. (b) Schematic diagram illustrating the preparation of the GONS–nHA complex using a wet chemical technique.

To initiate the process, a GO suspension with a  $0.05 \text{ g L}^{-1}$  concentration in a glass beaker was mixed with methanol, which was chosen based on its low values of dipole moment and  $-ve \zeta$  potential [22]. Next, 150 mL of homogenized GO suspension was subjected to ultrasonication treatment for 30 min using a tip sonicator at an amplitude of 22%. Then, the sonicated solution was removed, and the obtained GONSs were vacuum-filtered and dried. Upon drying, the GONSs were dispersed in distilled–deionized water at a concentration of  $0.5 \text{ mg/mL}$  and sonicated for 30 min to ensure a uniform distribution. A solution of 2.25 g of  $\text{Ca}(\text{NO}_3)_2 \cdot 4\text{H}_2\text{O}$  was dissolved in PBS. The  $\text{Ca}(\text{NO}_3)_2 \cdot 4\text{H}_2\text{O}$  solution was then mixed with the GONS suspension, and the pH of the mixture was adjusted to approximately 10 using a  $\text{NH}_4\text{OH}$  solution.

The mixture was placed in a  $60^\circ\text{C}$  water bath and stirred magnetically for 1.5 h to allow an adequate reaction between the carboxyl groups on GONSs and calcium ions

(Ca<sup>2+</sup>). A solution of (NH<sub>4</sub>)<sub>2</sub>HPO<sub>4</sub> was prepared by dissolving 0.75 g of (NH<sub>4</sub>)<sub>2</sub>HPO<sub>4</sub> in PBS, following a Ca/P molar ratio of 1.67. Dropwise, (NH<sub>4</sub>)<sub>2</sub>HPO<sub>4</sub> solution was added under continuous vigorous stirring of the GONS–Ca<sup>2+</sup> mixture at 50 °C for 6 h. After aging the resulting suspension at 35 °C for three days, the nHA–GONS suspension was vigorously stirred for 1 h. The rest was then filtered using a vacuum-assisted Buchner funnel and washed three times with 100 mL of deionized water to remove any remaining free GONSs and unmineralized nHA ions. Pure nHA whiskers were synthesized similarly, omitting the GONS step during the procedure.

## 2.2. Preparation and Characterization of PCL–nHA–GONS Composites

Initially, PCL was dissolved in DCM to make a 2% (*w/v*) PCL solution. The solution was stirred for 24 h using a magnetic stirrer to ensure that the PCL pellets were completely dissolved. PCL composites were prepared using 5, 10, and 20 weight percent (wt. %) nHA–GONSs and nHA. The naming convention (Table 1) for these samples was as follows: PGAP5, PGAP10, and PGAP20 for PCL–nHA–GONS composites and PHAP, PHAP5, PHAP10, and PHAP20 for nHA–PCL composites. The numerical suffixes in the sample names directly correspond to the respective weight percentages of the nanofillers in the composites.

**Table 1.** Nomenclature convention for PCL composites.

Sample	Nanofiller	Concentration %
PPCL	-	-
PHAP5	nHA	5
PHAP10	nHA	10
PHAP20	nHA	20
PGAP5	nHA–GONSs	5
PGAP10	nHA–GONSs	10
PGAP20	nHA–GONSs	20

Subsequently, a suspension of nHA and nHA–GONSs was gently added dropwise to the PCL–DCM solution. This suspension resulted in a coagulated composite, which then precipitated. Afterward, the composites were dried under a fume hood overnight at room temperature. Once dried, they were molded into films using a hot press. The films were approximately 200 µm thick and formed at 80 °C under a pressure of 10 MPa. A pure PCL film, devoid of any nanofiller, was also prepared using the same molding process as a comparative control. This control film served as a baseline for subsequent comparative analyses.

## 2.3. Morphological Analysis

Thermo Scientific Scios 2 Dual-Beam scanning electron microscopy (SEM) was used to analyze the blend and surface morphology of the scaffolds (8–10 images per sample) at an accelerating voltage of 5 kV. Samples were mounted on aluminum stubs using carbon tape and sputter-coated with a layer of gold with a thickness of 10 nm before imaging. A Thermo Scientific UltraDry Energy Dispersive Spectrometry (EDS) detector and Pathfinder software were used to analyze the elemental composition and distribution within the nHA–GONSs further on selected areas of the SEM images. The EDS elemental maps illustrate the spatial distributions of different elements.

## 2.4. Chemical Analysis

A LUMOS II Bruker Fourier transform infrared radiation (FTIR) microscope was used for chemical analysis. Samples were evaluated with the reflectance sampling technique. Each point was scanned 16 times with a resolution of 8 cm<sup>−1</sup>.

### 2.5. In Vitro Enzymatic Degradation

The enzymatic degradation of the scaffolds was studied using a lysozyme degradation test. The initial dry weight of the samples ( $W_i$ ) was recorded, followed by incubating them in the degradation media for hydrolysis (0.1 M PBS containing  $500 \mu\text{g mL}^{-1}$  of lysozyme at  $37^\circ\text{C}$ ) in an incubator. The membrane was removed from the degradation media, washed with distilled water, and weighed, while the extent of degradation was quantified as the change in sample weight over time. The percentage of weight loss was given by the following:

$$\frac{W_i - W_f}{W_i} \times 100 = W_{\text{loss}} \quad (1)$$

$W_i$  = initial weight;

$W_{\text{loss}}$  = weight loss percentage;

$W_f$  = final weight.

### 2.6. Thermal Characterization

The thermal behavior of the PGAP and PHAP membranes was tested using Perkin Elmer 4000 differential scanning calorimetry (Shelton, CT, USA). Samples were freeze-dried, crushed into a fine powder, weighed to 15–20 mg, and placed in aluminum pans. Samples were heated from  $20^\circ\text{C}$  to  $120^\circ\text{C}$  at a rate of  $5^\circ\text{C}/\text{min}$ , then held isothermally for 5 min to erase their thermal history. They were cooled to  $-10^\circ\text{C}$ . Nitrogen was used as the purge gas at a flow rate of  $\sim 20 \text{ mL}/\text{min}$ . Experiments were conducted in triplicate.

## 3. Results and Discussion

### 3.1. GONS Synthesis and Mineralization of nHA on GONSs

GONSs' formation mechanism and morphological details have been extensively studied, as reported in our previous research. In this investigation, a morphological analysis was conducted to assess the conversion of graphene nanoplatelets (GNPs) into graphene nanoscrolls (GNSs) [23]. The scanning electron microscope (SEM) images in Figure 1a,b depict the initial state of the GNPs and the subsequent formation of GONSs, respectively. The conversion of GO into GONSs is illustrated in Figure 1c–e, emphasizing the impact of physical treatment, particularly ultrasonication, on the wrinkled surface of graphene. A notably rough surface, attributed to ultrasonication, was observed, showcasing surface textures resembling short fibers. The fabrication of the GONSs was achieved through the LF ultrasonication of the GO suspension in methanol. The concentration of the GO suspension was meticulously selected based on factors such as the Hansen solubility parameter, the dipole moment of the solvent, and the zeta potential. Specifically, a concentration of  $0.05 \text{ g L}^{-1}$  of GO was chosen due to the lower negative zeta potential of the GO suspension, favoring the formation of GONSs. Sequential growth in the scrolling process is evident in the SEM images, illustrating the variable lengths and diameters of the GONSs.

The structural characteristics of the formed GONSs exhibit spindle and cylindrical (tubular) hollow geometries. Unlike GO nanosheets and carbon nanoscrolls, the GONSs exhibit distinctive behavior, characterized by excellent dispersion and minimal overlapping [18]. The adequate dispersion of GONSs provides a significant advantage for various applications, such as membrane fabrication, photocatalyst synthesis, and adsorption, by enhancing the active surface area or sites [14,18]. The ultrasonic pressure plays a crucial role in inducing unsteady bubble cavitation, including the nucleation, growth, and collapse of microscopic bubbles [14]. GO sheets efficiently utilize the energy provided by bubble cavitation to overcome the activation energy required for cross-scrolling, contributing to the fabrication of GONSs. The resulting GONSs exhibit concentric geometries with several distinct outer walls. The synthesis of nHA ( $\text{Ca}_{10}(\text{PO}_4)_6\text{OH}$ ) nanoparticles was conducted through the wet chemical method.  $\text{Ca}(\text{NO}_3)_2 \cdot 4\text{H}_2\text{O}$  and  $(\text{NH}_4)_2\text{HPO}_4$  were used as calcium and phosphate sources, respectively.  $\text{NH}_4\text{OH}$  was used as a precipitating agent. The overall reaction leading to the formation of nHA was as follows:

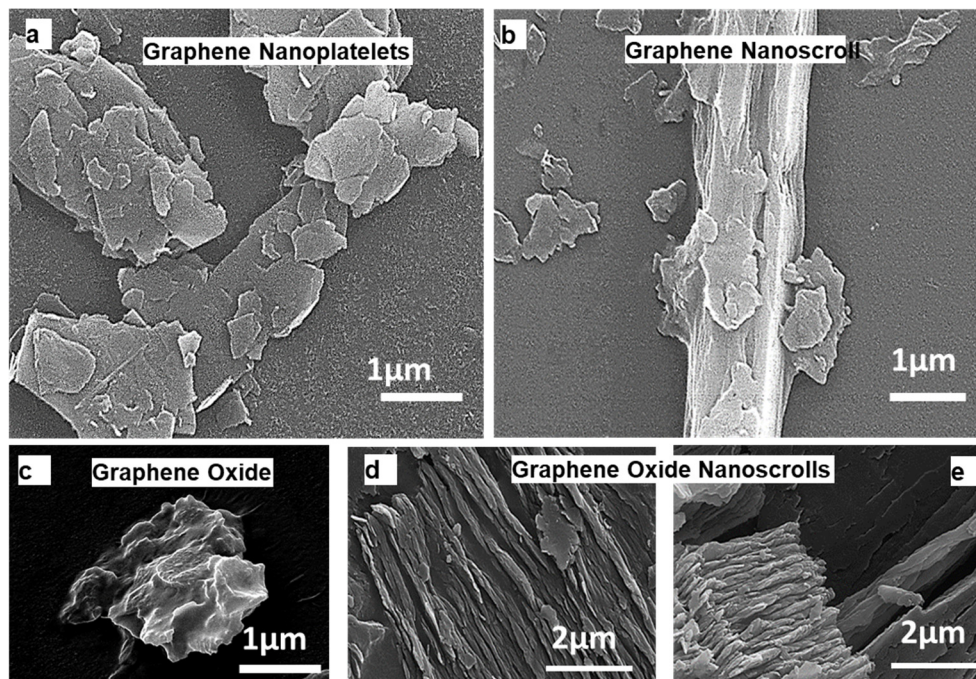


**Figure 1.** SEM images showcasing various graphene structures: (a) graphene nanoplatelets, (b) graphene nanoscrolls, (c) graphene oxide, and (d,e) graphene oxide nanoscrolls. ((a,b) reprinted with permission from Ref no. [23]).

SEM and EDS were utilized to investigate and confirm the formation of the nHA. The SEM (Figure 2a,b) images portray the clustered arrangement of the nHA and nHA-GONSSs.

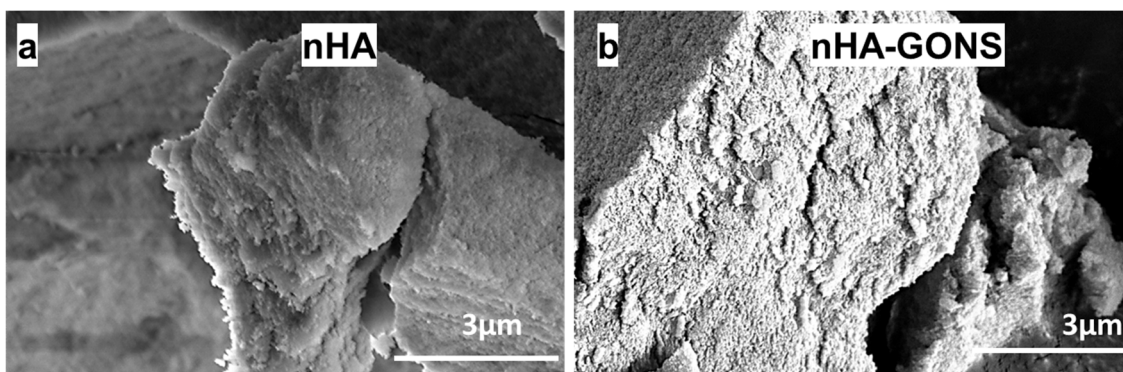


**Figure 2.** SEM images: (a) nHA and (b) composited nHA-GONSSs.

Furthermore, the EDS analysis (Figure 3a,d) revealed a Ca/P value of 1.71 for the synthesized nHA, showing a significant similarity to the Ca/P ratio observed in human bone [20,21]. The observed clustering is ascribed to Ostwald ripening because of the varying particle sizes of nHA synthesis arising from nucleation, where smaller nHA particles dissolve, releasing ions that preferentially deposit onto larger particles, leading to their growth and enhanced agglomeration [22–26].

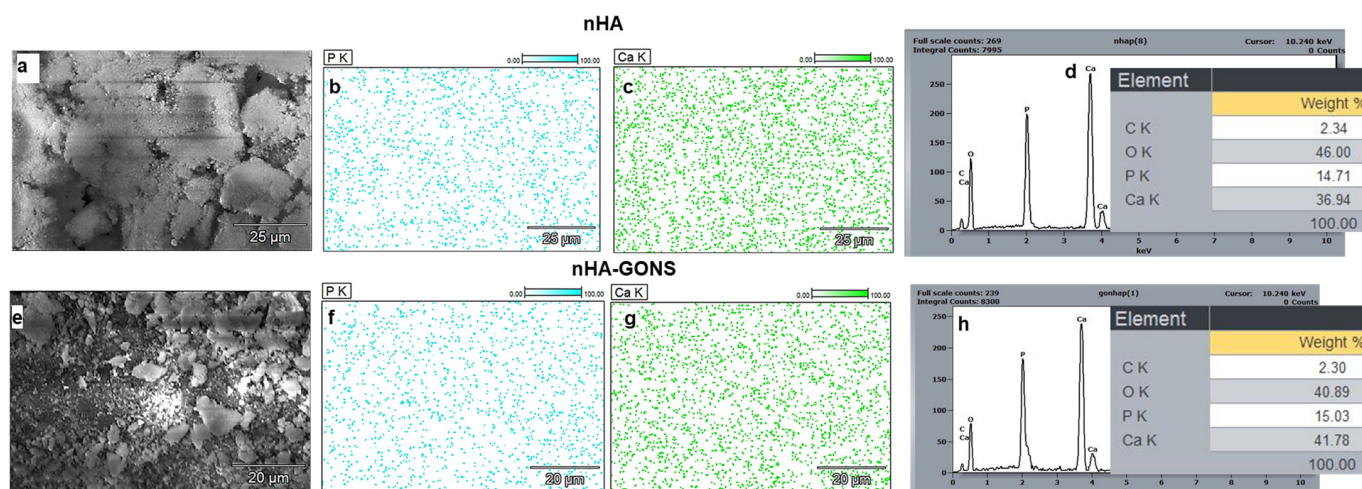


**Figure 3.** Comprehensive analysis of nHA and nHA–GONS surfaces: (a) SEM morphology of nHA; (b,c) EDS mapping of P and Ca adherence to nHA; (d) quantification of elemental weight percentages (C, O, P, Ca) on the nHA surface; (e) micrographs depicting the surface morphology of nHA–GONSs; (f,g) EDS analysis of P and Ca adherence to nHA–GONSs; and (h) corresponding elemental weight percentages (C, O, P, Ca) on the nHA–GONS surface.

The SEM and EDS (Figure 3e–h) of the nHA–GONSs, synthesized via the modified wet chemical method, reveal particles adhering almost uniformly to the surfaces of the GONSs. Despite rigorous washing procedures, nHA remained steadfastly affixed to the GONSs, underscoring the robust interface between GONSs and nHA and confirming the nucleating role of GONSs for the crystalline growth of nHA. Although GONSs were present at an ultralow concentration, their incorporation significantly assisted in the deposition of nHA on the surface of their surfaces, leading to uniform deposition with complete coverage of the GONSs. This deposition was mainly ascribed to the complete exfoliation of GONSs, which provided strong interfacial bonding for the as-formed nHA nanoparticles. It is important to note that nHA particles were selectively created and accommodated on the GONSs, arising from preferential nucleation and growth. This suggests that the presence of anionic functional groups in GONSs facilitates the nucleation of biominerals by attracting more  $\text{Ca}^{2+}$  cations to deposit onto their surface and subsequent biomineralization with  $\text{PO}_4^{3-}$ .

The spatial distribution (Figure 3) of Ca and P elements for nHA and nHA–GONSs displays a uniform distribution for all aspects, indicating the desirable structural homogeneity for the nHA–GONSs. The EDS spectra, moreover, showed some notable changes in the atomic weight proportions of nHA and nHA–GONSs, revealing an increase in the levels of P and Ca but decreases in oxygen after structural conjunction with the GONSs. In addition, the uniform elemental mapping distribution of the P and Ca elements implied that the nHA was uniformly dispersed in the GONS matrix. This observation suggests that the surface of the GONSs may be enveloped with an abundance of nHA. Furthermore, the Ca/P ratio of the apatite in the nHA–GONSs, calculated from the EDS spectrum (1.71), follows that of pure nHA. This characteristic aligns the chemical composition of the bone-like apatite in nHA–GONSs more closely with human biological apatite, rendering it promising for applications in bone tissue engineering [6].

Additionally, the presence of characteristic peaks at 1025, 960, and 640  $\text{cm}^{-1}$  in the nHA and nHA–GONSs, as shown in Figure 4, is indicative of the successful synthesis and retention of nHA's structural integrity when coupled with GONSs. These peaks are characteristic of phosphate vibrations in the HA crystal lattice, where the peak at 1025  $\text{cm}^{-1}$  corresponds to the  $\nu_3$  mode of  $\text{PO}_4^{3-}$  vibrations, the peak at 960  $\text{cm}^{-1}$  to the  $\nu_1$  mode of  $\text{PO}_4^{3-}$  stretching, and the peak at 640  $\text{cm}^{-1}$  to the  $\nu_4$  mode of  $\text{PO}_4^{3-}$  bending vibrations [27]. The presence of these peaks in both samples confirms the presence of

nHA. The higher absorbance observed in nHA compared to the nHA-GONSs suggests a difference in the packing density due to a more dispersed and less densely packed structure compared to nHA.

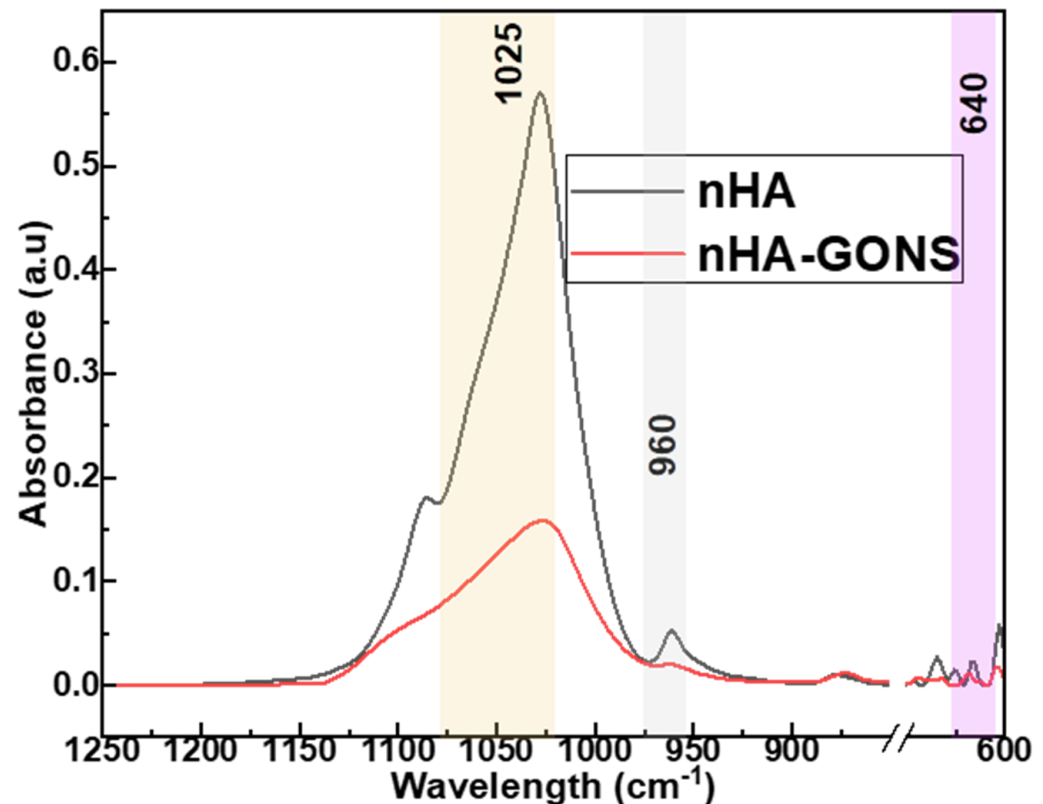
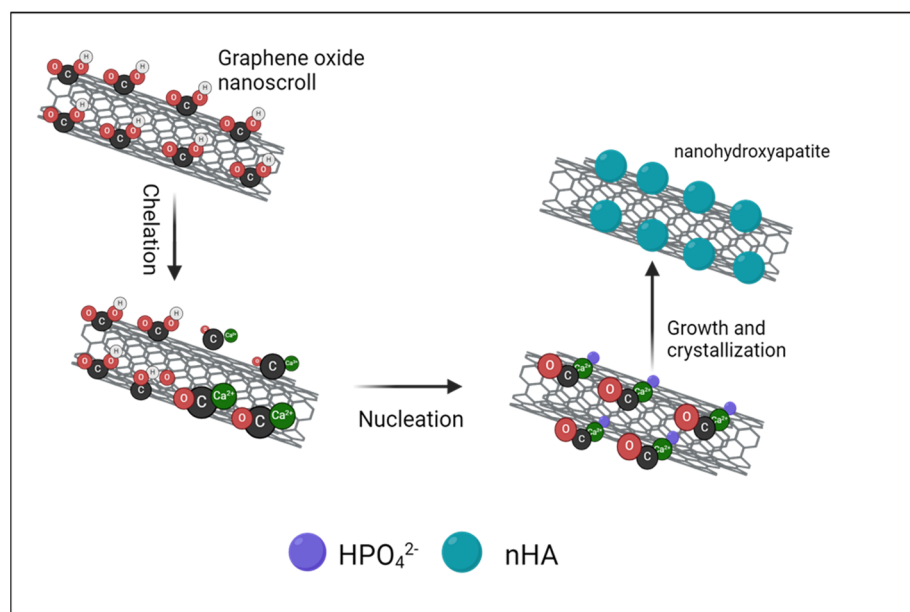


Figure 4. FTIR spectra for nHA and nHA-GONSs.

The GONSs' surface serves as a template for the oriented growth of nHA crystals, influencing their morphology and alignment [6]. The formation mechanism of nHA nanoparticles on the GONSs is presented in Figure 5. The GONSs possessed abundant oxygen-containing groups, including hydroxyl, epoxy, carboxyl, and carbonyl groups, which acted as anchor sites that induced the in situ growth of nHA on the GONSs. Studies have affirmed that oxygen-containing functional groups, such as  $-\text{COOH}$  or  $\text{COO}^-$ , can strongly interact with  $\text{Ca}^{2+}$  ions, facilitating nucleation and inducing the in situ growth of nHA through electrostatic interactions [12,24]. In the initial stage,  $\text{Ca}^{2+}$  was added to the sonicated GONS solution to chelate with the oxygen atoms of the epoxy groups and the carbonyl groups. The adsorption process is governed by the electrostatic interaction between the negatively charged GONS surface and the positively charged calcium cations on the (100) crystal plane of nHA. This electrostatic affinity leads to the effective binding of nHA onto the GONS surface, establishing a stable interface between the negatively charged GONSs and the positively charged nHA, thus influencing the dispersion and compatibility of nHA within the composite matrix [13,20,23]. Then,  $\text{HPO}_4^{2-}$ , formed by the dissolution of  $\text{Na}_2\text{HPO}_4$  under an alkaline environment, reacted with  $\text{Ca}^{2+}$  via electrovalent bonds. Therefore, many nHA nuclei were formed and uniformly distributed on the GONSs. As a result, the nHA nuclei gradually crystallized and grew onto the surface of the GONSs.



**Figure 5.** Elucidation of the formation mechanism of nHA crystals on GONSs, highlighting chelation, nucleation, and crystallization growth.

### 3.2. Scaffold Morphology

Figure 6a–g illustrate the surface morphologies of scaffolds with varying GONS content, with PCL scaffolds as the control. In the PHAP scaffolds (Figure 6b–d), the nHA particles exhibited a nonuniform distribution and agglomeration within the PCL matrix. In contrast, in the PGAP scaffolds, the extent of aggregation diminished with increasing GO content (Figure 5e–g). PCL typically exhibits poor interfacial bonding with nHA due to inherent differences in their chemical and physical properties. PCL is a hydrophobic aliphatic polyester with relatively low surface energy, while nHA is an inorganic, hydrophilic material with a high surface energy [7,28]. These polarity and surface energy differences result in a limited affinity between PCL and nHA. The hydrophobic nature of PCL hinders its effective interaction with the hydrophilic surface of nHA, leading to poor wetting and adhesion.

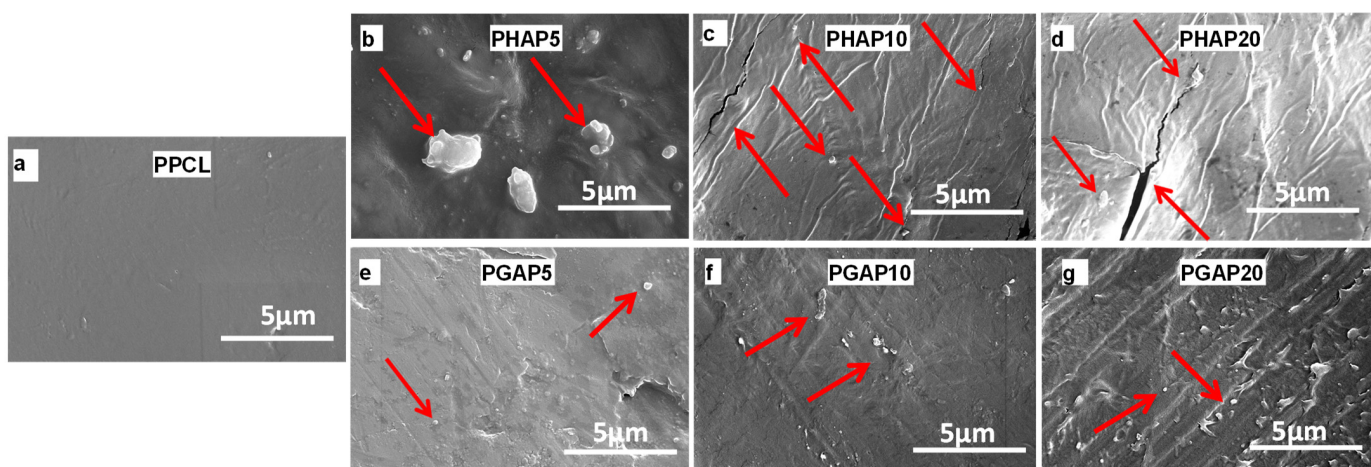


**Figure 6.** SEM images depicting polycaprolactone composites with nanofillers: (a) control without nanofiller; (b–d) nHA at 5%, 10%, and 20% concentrations; and (e–g) nHA–GONSs at 5%, 10%, and 20% concentrations (arrows indicate nHA particles.).

GO is prone to aggregation when mixed with polymers. GO tends to form irreversible agglomerates in the polymer matrix due to the strong van der Waals force among them.

However, for the nHA–GONS nanocomposite produced by the in situ growing method, nHA uniformly grew on the surface of the GONSs. By being inserted into the scrolls of the GONSs, nHA reduced the stacking of GONSs. Therefore, nHA nanoparticles and GONSs formed a synergistic system that supported each other to minimize aggregation and promote dispersion.

An enhancement in the interfacial bonding strength is manifested through the dispersibility and compatibility of the PGAP scaffolds. Despite PCL's aliphatic nature being devoid of a traditional conjugated  $\pi$ -system, the combination of van der Waals forces and hydrogen bonding establishes robust interactions between PCL and the scrolled GONS structure. Concurrently, hydrogen bonding, facilitated by ester groups in the PCL and oxygen functionalities in the GONSs, contributes to the stable adsorption of PCL onto the scrolled GONSs. This intricate interplay between van der Waals forces and hydrogen bonding enhances the overall compatibility between the aliphatic PCL chains and the scrolled graphene-based structure of the GONSs. The resulting composite material exhibits improved dispersion of nHA within the PCL matrix.

Additionally, GONSs carry a negative charge owing to their abundant oxygen functional groups (carboxylic acids and hydroxyls). Upon composite formation, the positively charged calcium cations are adsorbed onto the negatively charged GONS surfaces through electrostatic interactions. Consequently, facilitated by the influence of GONSs, nHA achieves uniform dispersion in the PCL matrix, thereby enhancing the compatibility between nHA and PCL.

### 3.3. Chemical Analysis

An ATR-FTIR analysis was carried out for the surface characterization of PCL and PCL–nHA–GONSs before and after biomineralization. Figure 6a–c show the FTIR spectra of pure PCL and the PCL–nHA, and PCL–nHA–GONS composites. The absorption bands observed in the PCL–nHA–GONSs located at  $1725\text{ cm}^{-1}$  (carbonyl stretching),  $1290\text{ cm}^{-1}$  (C–O and C–C stretching), and  $1193$  and  $1162\text{ cm}^{-1}$  (asymmetric C–O–C stretching) are characteristic of the absorption of PCL. Furthermore, the bands at  $960$  and  $1042\text{ cm}^{-1}$  represent the asymmetric stretching vibrations of P–O in  $\text{PO}_4^{3-}$  groups, while the bands at  $730\text{ cm}^{-1}$  are ascribed to the bending vibrations of O–P–O in  $\text{PO}_4^{3-}$  groups.

The FTIR spectroscopy (Figure 7a) and DSC measurements revealed close interactions between the nHA–GONSs and the PCL chains, providing valuable insights into polar interactions, segmental mobility, and crystal thermostability. The characteristic bands of the PCL–nHA–GONSs showed exclusive blue shifts and band splitting, while the prominent bands of the PCL–nHA composite were similar to those of pure PCL. Specifically, the bands assigned to  $\text{CH}_3$  asymmetric stretching ( $2995\text{ cm}^{-1}$ ) in the pure PCL shifted to  $2942$  and  $2862\text{ cm}^{-1}$  for all the PCL–nHA–GONS-filled composites, indicating the conformational ordering of the PCL chains in the presence of the nHA–GONSs. These blue shifts were likely due to the carbonyl groups in the PCL backbone acting as dipoles, allowing for dipole–dipole interactions with the polar groups on the GONSs; these interactions can contribute to the affinity between PCL and GONSs.

At the  $\text{CH}_3$  asymmetric stretching peak ( $2942\text{ cm}^{-1}$ ), the intensity is lower for pure PCL, serving as the baseline reference. PHAP5 and PHAP10 display a slight increase in intensity compared to pure PCL. In contrast, the PGAP series (PGAP20, PGAP10, and PGAP5) shows similar intensities but notably higher absorbance values than PHAP5 and PHAP10. The highest absorbance is observed for PHAP20. A similar trend is observed at the C–H stretching peak ( $2862\text{ cm}^{-1}$ ); PHAP5 and PHAP10 exhibit higher intensities than the PGAP series, with pure PCL showing the lowest intensity. This suggests that the incorporation of GONSs at different concentrations (5%, 10%, and 20%) modifies the intensity and absorbance characteristics compared to pure PCL and PHAP. The variations in the peak intensities at  $2942\text{ cm}^{-1}$  and  $2862\text{ cm}^{-1}$  may be attributed to the interactions between the PCL, nHA, and GONSs in the composites. The increased intensity for PHAP5 and PHAP10 indicates the potential influence of nHA on the  $\text{CH}_3$  asymmetric stretching

peak. Despite varying concentrations, the consistent intensity in the PGAP series implies that GONSs may play a dominant role in determining the absorbance at these peaks. GONSs and nHA could act synergistically as nucleating agents, promoting the formation of more crystalline domains within the PCL matrix. This enhanced crystallinity results in higher peak intensities due to the more efficient packing of polymer chains, which enhances the vibrational modes detected by FTIR. The initial high intensity observed for PGAP20 suggests that the composite structure, influenced by the optimal dispersion and nucleation effect of nHA–GONSs, presents a compact and well-ordered arrangement that maximizes the absorbance of peaks.

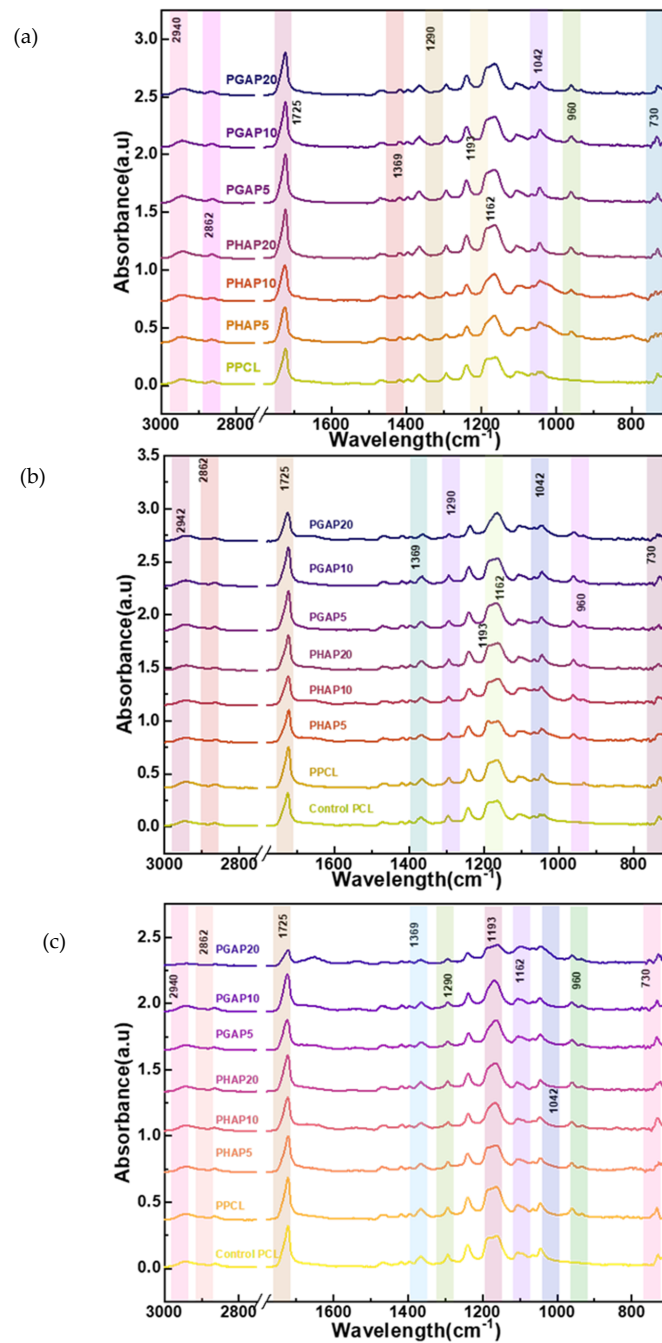


**Figure 7.** FTIR spectra for PCL and nHA and the PCL–nHA, and PCL–nHA–GONS composites: (a) pre-degradation; (b) after 14 days of enzymatic degradation; and (c) after 21 days of enzymatic degradation.

After 14 days of enzymatic degradation, a decrease in intensity for all major peaks was observed (Figure 7b). The control and degraded pure PCL samples exhibited the highest intensities at the CH<sub>3</sub> asymmetric stretching peak (2942 cm<sup>-1</sup>) and the reported peaks pre-degradation compared to the PHAP and PGAP series. This trend suggests significant alterations in the PCL structure during prolonged exposure. The PGAP series, particularly PGAP20, displayed the lowest intensities for this peak after degradation. This unexpected behavior may be due to the GONSs' scrolled structure. Similarly, both the control and degraded pure PCL samples had the highest intensities at the carbonyl stretching peak (1725 cm<sup>-1</sup>) after 21 days of enzymatic degradation (Figure 7c). Both the control and degraded pure PCL samples had similar intensities at the C-O and C-C stretching peaks (1290 cm<sup>-1</sup>) after 21 days. Pure PCL lacks the additional interfaces and potential stress concentration points introduced by the nHA and nHA-GONSs. This absence results in a more uniform degradation process, primarily governed by the hydrolysis of ester linkages.

The PGAP series, particularly PGAP20, had the lowest intensities for this peak after degradation, followed by PGAP10 and PGAP5. PGAP20 had the lowest intensities for the asymmetric C-O-C stretching peaks (1193 and 1162 cm<sup>-1</sup>) after 21 days. The PHAP series also showed similar trends to the PGAP, with differences only in the intensity after degradation. The distinct behavior observed in the PGAP series, particularly with PGAP20 exhibiting the lowest FTIR intensities post-degradation, underscores the unique influence of nHA-GONSs on the enzymatic degradation of PCL composites. This trend is primarily attributed to the scrolled structure of GONSs, which plays a pivotal role in enzyme retention within the composite matrix. Due to their unique morphology, GONSs act as physical barriers that may impede direct enzymatic access to PCL chains and create microenvironments conducive to retaining enzymes. This retention can lead to a sustained interaction between the enzymes and the PCL substrate, potentially enhancing the degradation process even after initial exposure to degradative conditions has ceased.

The continuous degradation observed in the PGAP composites suggests that the incorporation of GONSs facilitates a different mechanism of degradation compared to traditional composite formulations. While the physical barrier formed by GONSs could be expected to protect the PCL matrix by limiting enzyme penetration, the retention of enzymes within the scrolled structures appears to prolong the enzymatic action on PCL. This mechanism leads to a sustained or possibly accelerated degradation over time, as evidenced by the reduced FTIR intensities, particularly in the asymmetric C-O-C stretching regions, indicative of alterations in the molecular structure and vibrational modes of PCL. This enzyme retention capability of the GONSs, resulting in sustained enzymatic degradation, marks a significant departure from the behavior of the composites without GONSs or those with nHA alone.

### 3.4. Thermal Analysis

The investigation into the thermal properties of the composite scaffolds, as depicted in Figure 8, revealed noteworthy trends in the melting temperature (T<sub>m</sub>) and crystallization temperature (T<sub>c</sub>).

While T<sub>m</sub> values exhibited some variability across the different compositions, no consistent upward or downward trend was observed with the addition of the nHA-GONSs. An overall crystallization temperature (T<sub>c</sub>) increase was discerned in the presence of both the nHA and nHA-GONSs compared to the control PCL scaffold. This elevation in T<sub>c</sub> is commonly associated with nucleation effects from both nHA and nHA-GONSs, influencing crystallization by providing sites for polymer chain organization. The augmented content of nHA and nHA-GONSs in the composite was found to impede the regular rearrangement of PCL macromolecules during crystallization, restricting the mobility of PCL chains within the composite and consequently leading to reduced crystallization.

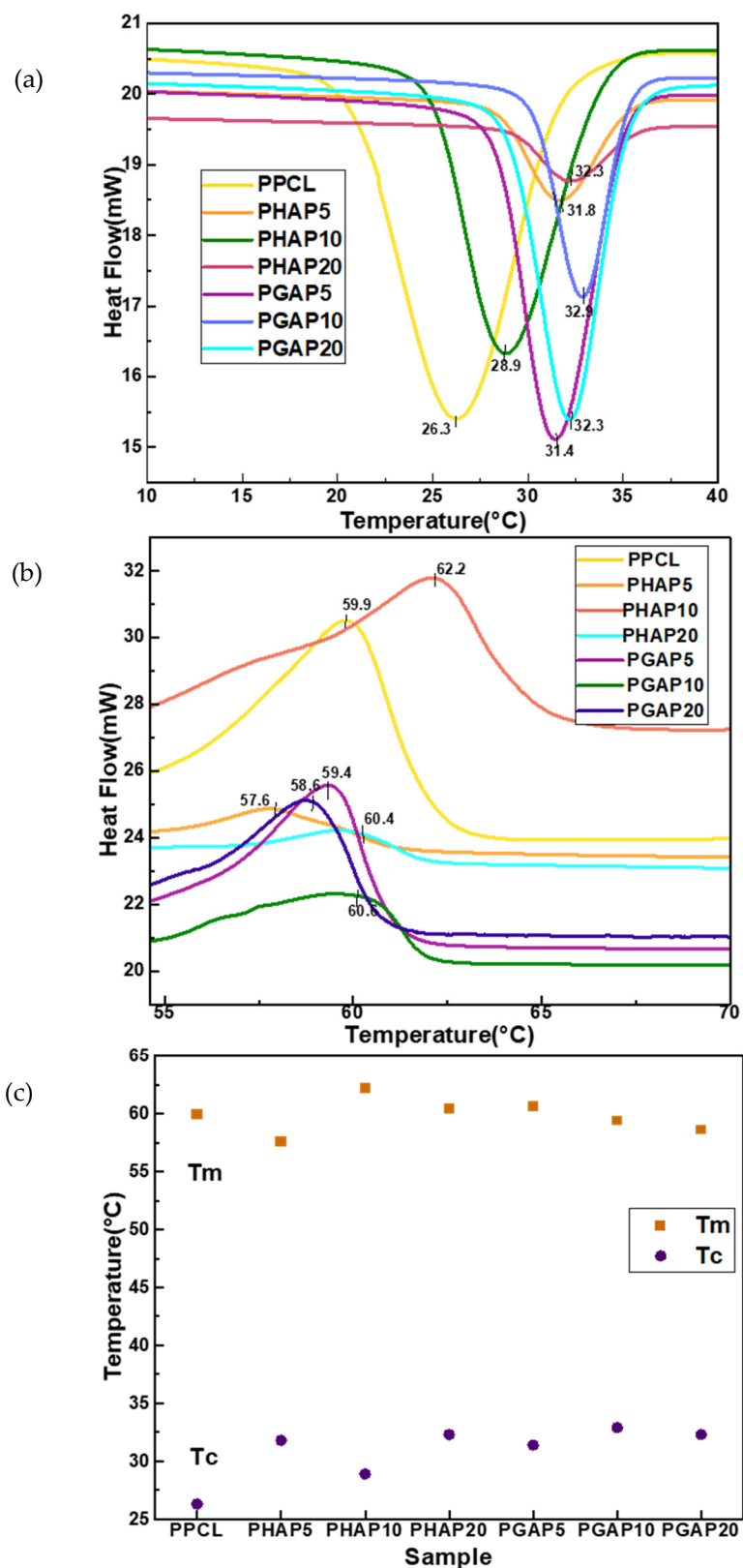


**Figure 8.** Differential scanning calorimetry models for PCL composites: (a) cooling curve; (b) heating curve; and (c) overview of thermal properties.

Furthermore, the observed increase in the crystallization temperature ( $T_c$ ) is desirable for enhanced thermal stability and resistance to deformation; this is particularly advantageous in load-bearing scenarios, where improved dimensional stability of PCL is crucial.

The substantial rise in  $T_c$  noted in the PGAP series, compared to that in the PHAP series, is attributed to the robust interfacial bonding facilitated by the GONSs. The scrolled structure of GONSs, exposing numerous bonding groups, enhances compatibility between the polymer matrix and reinforcing agents like nHA.

This compatibility, along with the nucleating effects of GONSs, results in restrained molecular mobility during crystallization, fostering a more ordered arrangement in the polymer matrix and contributing to the observed elevation in  $T_c$ . The intricate interplay of GONSs, characterized by their scrolled architecture, their exposed bonding groups, and their combinatorial nucleating effect, underscores the pivotal role of interfacial bonding in influencing the crystallization behavior of composite materials.

Table 2 shows the variations in the enthalpies of fusion and crystallization, revealing crucial insights into the molecular interactions and arrangement of polymer chains. In PPCL, the lower enthalpies of fusion and crystallization suggest a polymer matrix with less organized and tightly packed chains. As a result, the melting and crystallization processes require less energy.

**Table 2.** Thermodynamic data: heat of fusion and heat of crystallization.

Sample	Enthalpy of Fusion (J/g)	Enthalpy of Crystallization (J/g)
PPCL	9.8	−10.1
PHAP5	8.6	−3.9
PHAP10	12.3	−12.9
PHAP20	13.3	−2.7
PGAP5	37.0	−42.8
PGAP10	44.6	−42.1
PGAP20	53.2	−52.3

The introduction of nHA in the PHAP series, without GONSs, brings about interesting changes. The negative enthalpies of crystallization indicate an endothermic process, possibly suggesting enhanced crystallinity due to the presence of nHA. In the PGAP series, the inclusion of GONSs along with nHA leads to increased enthalpies of fusion, indicating a higher energy requirement for melting. This implies enhanced interactions between the polymer chains and nanofillers, resulting in a more stable composite structure. The negative enthalpies of crystallization in the PGAP series suggest an exothermic crystallization process, possibly influenced by the unique structure and surface chemistry of GONSs.

This facilitates more efficient nucleation and the growth of crystalline structures. The observed trends suggest the potential formation of a more organized and stable polymer structure in the presence of GONSs. Additionally, the variations in the enthalpies of fusion and crystallization signify changes in polymer chain interactions, crystalline arrangements, and energy transfer mechanisms. Higher enthalpies of fusion and crystallization indicate stronger intermolecular interactions. The enthalpy of fusion, representing the energy needed for a solid-to-liquid transition, reflects the need to overcome intermolecular forces, implying stronger bonds in the solid phase. Conversely, the enthalpy of crystallization, indicating the heat released during a liquid-to-solid transition, signifies stronger intermolecular interactions in the solid state, leading to an exothermic process. Therefore, higher enthalpies of fusion and crystallization suggest more robust intermolecular bonds in the PGAP series, influencing its stability and performance in varying temperature conditions.

### 3.5. *In Vitro* Degradation

Figure 9 illustrates the enzymatic degradation of different samples after two and three weeks. After two weeks, PPCL showed the highest weight loss at 2.5%, indicating its susceptibility to enzymatic degradation.

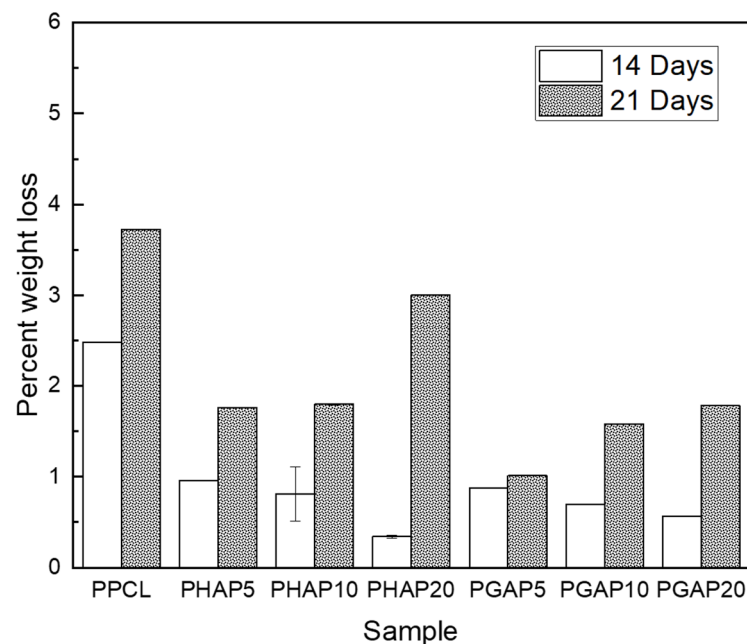


**Figure 9.** Comparative assessment of in vitro enzymatic degradation, presenting the average percent weight loss for each composite after 14 and 21 days.

In contrast, PHAP5, PHAP10, and PHAP20, which contained nHA, experienced weight losses of 1%, 0.8%, and 0.5%, respectively. Interestingly, PGAP5, PGAP10, and PGAP20, which incorporated nHA–GONSs, showed lower weight losses of 1%, 0.8%, and 0.3%, respectively. After three weeks, PPCL still had the highest weight loss at 3.6%, while PHAP5, PHAP10, and PHAP20 had weight losses of 1.8%, 2.0%, and 2.9%, respectively. For PGAP5, PGAP10, and PGAP20, the weight losses were 1%, 1.5%, and 1.8%, respectively.

After 21 days, there was a clear trend of increased weight loss across all the scaffolds compared to the earlier 14-day period, indicating an acceleration in degradation. This trend can be attributed to the weakening of the PCL matrix as degradation progresses. Initially, the integrity of the scaffold supports slower degradation rates, but as the matrix begins to break down, its structural weaknesses allow for faster penetration and the action of enzymes and water, leading to a more rapid loss in mass. The PHAP20 and PGAP20 samples showed particularly significant increases in weight loss, suggesting that higher nanofiller concentrations in these polymers might catalyze the degradation process. Additionally, the PHAP series generally exhibited more weight loss than the PGAP series, highlighting the reinforcement brought on by the GONSs.

Regarding the weight loss of PCL over time, incorporating GONSs is expected to mitigate the degradation process. PPCL exhibits the highest weight loss, likely due to the susceptibility of PCL to lysozyme hydrolysis. Due to nHA's intrinsic stiffness, increased concentrations of nHA in the PHAP series resulted in a more rigid structure. However, this rigidity introduces stress concentration points, particularly where nHA particles agglomerate, which accelerates degradation under physiological conditions by creating localized environments conducive to hydrolysis. In addition, agglomerations hinder efficient water drainage from localized points with elevated fluid and enzyme content. Localized water-rich environments near agglomerates allow for a greater exposure of PCL to water molecules. In contrast, the PGAP scaffolds demonstrated enhanced resistance to degradation due to the protective role of GONSs. The scrolling is a physical barrier, preventing lysozyme penetration and reducing PCL's exposure to enzymatic hydrolysis. The strong interfacial bonding and improved dispersion of the composite scaffold act as protective mechanisms, slowing down the degradation kinetics of PCL.

EDS mapping was conducted on the surfaces of the scaffolds after fabrication to examine the difference in the calcium ion intensities between the PHAP and PGAP scaffolds.

Among the PHAP series, PHAP10 and PHAP20 showed visibly lower intensities than PHAP5. In contrast, the calcium ion intensity on the PGAP scaffolds remained constant across the different concentrations. The EDS maps (Figure 10) provide a clear view of the elemental composition changes during 14 of the 21-day enzymatic degradation period. Before degradation, both PGAP and PHAP exhibited similar  $\text{Ca}^{2+}$  dynamics. However, there was a noticeable difference in the preservation of  $\text{Ca}^{2+}$  between PHAP and PGAP. The PGAP series demonstrated a significant preservation of  $\text{Ca}^{2+}$ , while the PHAP samples showed a noticeable loss in  $\text{Ca}^{2+}$ .

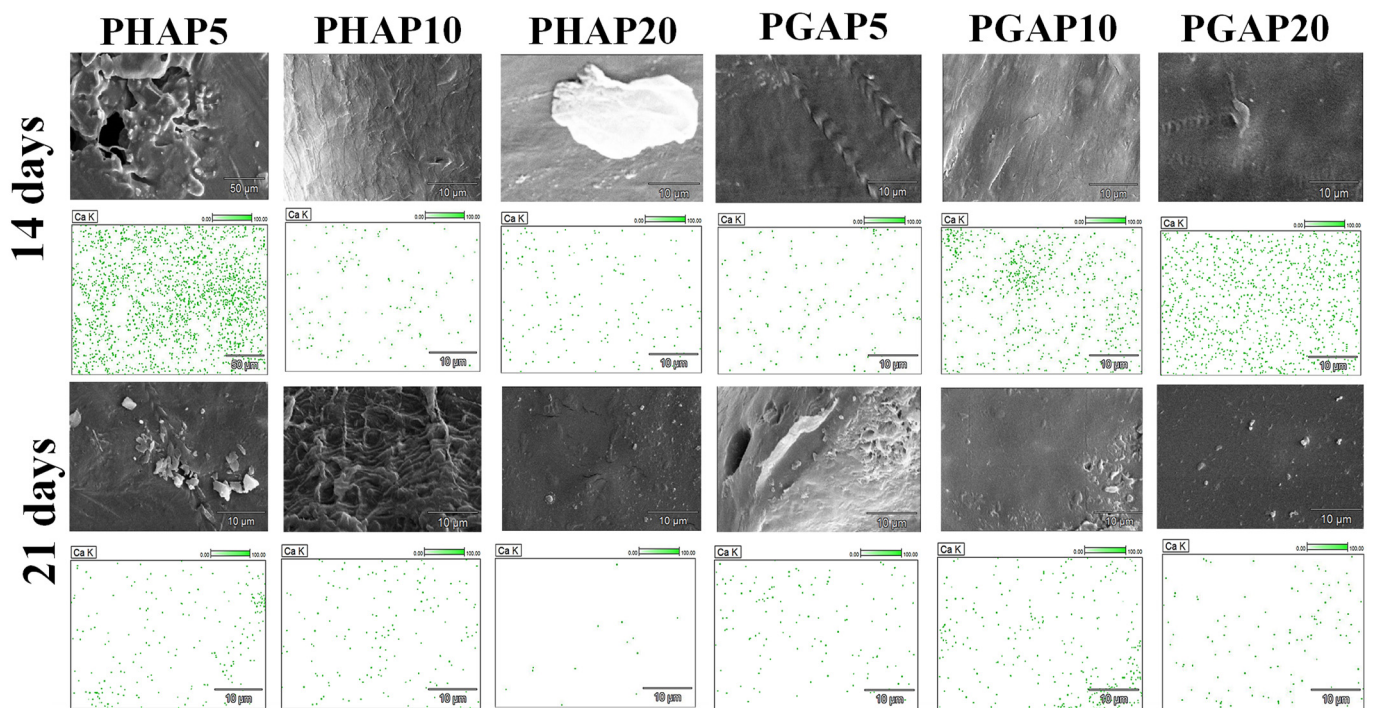


**Figure 10.** EDS analysis of oxygen, phosphorus, and calcium surface adherence after 14- and 21-days of in vitro degradation for the PCL composites.

After 14 days of exposure to lysozyme in PBS, all the samples showed a decline in Ca ion intensity. The sample with a higher concentration of PGAP maintained higher intensities compared to all the PHAP samples. After 21 days (Figure 10), PHAP10 and PHAP20 exhibited a significant reduction in calcium ion intensity, while PGAP10 and PGAP20 retained the highest intensities. This suggests that PGAP scaffolds have unique stability and resistance to degradation, highlighting the potential benefits of incorporating GONSs to enhance the interfacial bonding between PCL and nHA in enzymatic environments.

The SEM images revealed a distinct pattern of surface erosion on the PHAP5 scaffold during the degradation period, leading to an increased exposure of calcium ions on the surface. This erosion can be attributed to the specific degradation behavior of PHAP5 under enzymatic conditions. It indicates that the degradation process mainly affects the outer layer of the scaffold, resulting in the release and exposure of calcium ions. The absence of visible cracks suggests that degradation primarily occurs through surface erosion rather than bulk degradation, allowing potential interactions with the surrounding environment.

After 21 days of enzymatic degradation, distinct changes in surface morphology were observed in each sample. The SEM and EDS images (Figure 10) revealed agglomeration and an increased exposure of calcium ions on the surface of PHAP5. This agglomeration could indicate localized concentration changes in the degradation byproducts, and the ongoing exposure of calcium ions may contribute to the scaffold's bioactive properties. PHAP10 displayed a very rough and eroded surface after 21 days of degradation. This increased roughness may be associated with a more aggressive degradation process or a different degradation pathway than that of PHAP5 due to agglomerations. Agglomeration

is associated with poor mechanical properties because these loosely bound clusters of nanoparticles lead to an uneven stress distribution and reduced effective interactions with the PCL composite matrix. This results in decreased reinforcement efficiency, increased susceptibility to mechanical failure, and compromised composite structural integrity [29].

The diverse oxygen functional groups on GONSs, including hydroxyl, epoxy, and carboxyl groups, orchestrate intricate interactions with PCL and nHA. The hydroxyl groups on GONSs promote hydrogen bonding and dipole–dipole interactions, establishing strong connections with the carbonyl groups in PCL and the hydroxyl groups in nHA. This interaction ensures the uniform dispersion of GONSs, promoting a well-integrated composite structure. This dual interaction facilitates the effective integration of GONSs, PCL, and nHA, allowing for better anchoring of  $\text{Ca}^{2+}$  ions during degradation. The resulting PGAP composite scaffolds exhibit superior capabilities in retaining calcium ions during enzymatic degradation compared to the PHAP scaffolds. The robust interfacial bonding and uniform dispersion provided by the GONSs contribute to enhanced resistance to degradation. Retaining calcium ions on the surface of the hydroxyapatite scaffold supports the deposition of minerals and the formation of a mineralized matrix, contributing to the development of new bone tissue.

#### 4. Conclusions

Bioactive PCL and PCL–nHA–GONS nanohybrids were synthesized using hot press molding, leveraging the exceptional properties of GONSs. The wrinkled morphology and strong interfacial interactions, as indicated by the new FTIR absorption peaks associated with hydrogen bonding, further contributed to the enhanced properties of the nHA–GONSs. In the biomineralization experiments with PBS, the GONSs demonstrated a facilitative role in the nucleation of calcium phosphate on PCL membranes, owing to their anionic functional groups. The graphene-oxide-templated synthesis elucidated the preferential nucleation and accommodation of nHA on the GONSs' surfaces. The resulting nHA–GONSs exhibited strong interactions due to abundant oxygen functional groups, ensuring good exfoliation and intimate integration within the PCL matrix. The unique concentric geometries of GONSs, coupled with their resistance to aggregation, render them advantageous for a range of applications. Notably, the oxygen-containing functional groups on the GONSs facilitated strong interactions with  $\text{Ca}^{2+}$  ions, promoting nucleation and mineralization. The substantial specific surface area of the GONSs provided an extensive platform for ion anchoring. The resulting PGAP composite scaffolds exhibited enhanced interfacial bonding, addressing the inherent poor bonding between PCL and nHA observed in the PHAP scaffolds. The surface morphologies of the PGAP scaffolds illustrated a reduced agglomeration of nHA particles, further enhancing the interfacial compatibility between the components in the composite scaffolds.

**Author Contributions:** Conceptualization, L.T.M. and D.D.; methodology, L.T.M.; software, L.T.M.; validation, L.T.M. and D.D.; formal analysis, L.T.M.; investigation, D.D.; data curation, L.T.M., J.S. and G.B.; writing—original draft preparation, L.T.M.; writing—review and editing, L.T.M. and D.D.; visualization, D.D.; supervision, D.D.; project administration, D.D.; funding acquisition, D.D. All authors have read and agreed to the published version of the manuscript.

**Funding:** This research was supported by the Louisiana Board of Regents Support Fund, RCS project, contract number: LEQSF (2020-23)-RD-A-21.

**Institutional Review Board Statement:** Not applicable.

**Data Availability Statement:** Data are contained within the article.

**Conflicts of Interest:** The authors declare no conflicts of interest. The funders had no role in the design of the study; in the collection, analyses, or interpretation of data; in the writing of the manuscript; or in the decision to publish the results.

## References

1. Amini, A.R.; Laurencin, C.T.; Nukavarapu, S.P. Bone Tissue Engineering: Recent Advances and Challenges. *Crit. Rev. Biomed. Eng.* **2012**, *40*, 363–408. [[CrossRef](#)]
2. Mondal, D.; Griffith, M.; Venkatraman, S.S. Polycaprolactone-based biomaterials for tissue engineering and drug delivery: Current scenario and challenges. *Int. J. Polym. Mater. Polym. Biomater.* **2016**, *65*, 255–265. [[CrossRef](#)]
3. Dwivedi, R.; Kumar, S.; Pandey, R.; Mahajan, A.; Nandana, D.; Katti, D.S.; Mehrotra, D. Polycaprolactone as biomaterial for bone scaffolds: Review of literature. *J. Oral Biol. Craniofacial Res.* **2020**, *10*, 381–388. [[CrossRef](#)] [[PubMed](#)]
4. Bartnikowski, M.; Dargaville, T.R.; Ivanovski, S.; Hutmacher, D.W. Degradation mechanisms of polycaprolactone in the context of chemistry, geometry and environment. *Prog. Polym. Sci.* **2019**, *96*, 1–20. [[CrossRef](#)]
5. Hou, Y.; Wang, W.; Bartolo, P. Investigation of polycaprolactone for bone tissue engineering scaffolds: In vitro degradation and biological studies. *Mater. Des.* **2022**, *216*, 110582. [[CrossRef](#)]
6. Peng, S.; Feng, P.; Wu, P.; Huang, W.; Yang, Y.; Guo, W.; Gao, C.; Shuai, C. Graphene oxide as an interface phase between polyetheretherketone and hydroxyapatite for tissue engineering scaffolds. *Sci. Rep.* **2017**, *7*, 46604. [[CrossRef](#)]
7. Ferroni, L.; Gardin, C.; Rigoni, F.; Balliana, E.; Zanotti, F.; Scatto, M.; Riello, P.; Zavan, B. The Impact of Graphene Oxide on Polycaprolactone PCL Surfaces: Antimicrobial Activity and Osteogenic Differentiation of Mesenchymal Stem Cell. *Coatings* **2022**, *12*, 799. [[CrossRef](#)]
8. Fu, S.; Ni, P.; Wang, B.; Chu, B.; Peng, J.; Zheng, L.; Zhao, X.; Luo, F.; Wei, Y.; Qian, Z. In vivo biocompatibility and osteogenesis of electrospun poly( $\epsilon$ -caprolactone)–poly(ethylene glycol)–poly( $\epsilon$ -caprolactone)/nano-hydroxyapatite composite scaffold. *Biomaterials* **2012**, *33*, 8363–8371. [[CrossRef](#)]
9. Chuenjittakuntaworn, B.; Inrung, W.; Damrongsri, D.; Mekaapiruk, K.; Supaphol, P.; Pavasant, P. Polycaprolactone/hydroxyapatite composite scaffolds: Preparation, characterization, and in vitro and in vivo biological responses of human primary bone cells. *J. Biomed. Mater. Res. Part A* **2010**, *94*, 241–251. [[CrossRef](#)]
10. Cardoso, G.; Tondon, A.; Maia, L.; Cunha, M.; Zavaglia, C.; Kaunas, R. In vivo approach of calcium deficient hydroxyapatite filler as bone induction factor. *Mater. Sci. Eng. C* **2019**, *99*, 999–1006. [[CrossRef](#)]
11. Milovac, D.; Ferrer, G.G.; Ivankovic, M.; Ivankovic, H. PCL-coated hydroxyapatite scaffold derived from cuttlefish bone: Morphology, mechanical properties and bioactivity. *Mater. Sci. Eng. C* **2014**, *34*, 437–445. [[CrossRef](#)] [[PubMed](#)]
12. Iswarya, S.; Theivasanthi, T.; Chinnaiyah, K.; Gopinath, S.C. Theivasanthi, K. Chinnaiyah, Subash C.B. Gopinath. Sodium alginate/hydroxyapatite/graphene nanoplatelets composites for bone tissue engineering. *Appl. Nanosci.* **2024**, *14*, 109–122. [[CrossRef](#)]
13. Cui, W.; Li, X.; Zhou, S.; Weng, J. *In situ* growth of hydroxyapatite within electrospun poly(DL-lactide) fibers. *J. Biomed. Mater. Res. Part A* **2007**, *82*, 831–841. [[CrossRef](#)]
14. Xiao, Y.; Gong, T.; Zhou, S. The functionalization of multi-walled carbon nanotubes by in situ deposition of hydroxyapatite. *Biomaterials* **2010**, *31*, 5182–5190. [[CrossRef](#)] [[PubMed](#)]
15. Marrella, A.; Aiello, M.; Quarto, R.; Scaglione, S. Chemical and morphological gradient scaffolds to mimic hierarchically complex tissues: From theoretical modeling to their fabrication. *Biotechnol. Bioeng.* **2016**, *113*, 2286–2297. [[CrossRef](#)] [[PubMed](#)]
16. Li, D.; Chen, M.; Guo, W.; Li, P.; Wang, H.; Ding, W.; Li, M.; Xu, Y. In Situ Grown Nanohydroxyapatite Hybridized Graphene Oxide: Enhancing the Strength and Bioactivity of Polymer Scaffolds. *ACS Omega* **2022**, *7*, 12242–12254. [[CrossRef](#)] [[PubMed](#)]
17. Núñez, J.D.; Benito, A.M.; González, R.; Aragón, J.; Arenal, R.; Maser, W.K. Integration and bioactivity of hydroxyapatite grown on carbon nanotubes and graphene oxide. *Carbon* **2014**, *79*, 590–604. [[CrossRef](#)]
18. Sontakke, A.D.; Purkait, M. Fabrication of ultrasound-mediated tunable graphene oxide nanoscrolls. *Ultrason. Sonochemistry* **2020**, *63*, 104976. [[CrossRef](#)] [[PubMed](#)]
19. Cojocar, E.; Ghitman, J.; Biru, E.I.; Pircalabioru, G.G.; Vasile, E.; Iovu, H. Synthesis and Characterization of Electrospun Composite Scaffolds Based on Chitosan-Carboxylated Graphene Oxide with Potential Biomedical Applications. *Materials* **2021**, *14*, 2535. [[CrossRef](#)]
20. Kausar, A. Nanoscrolls of graphene and graphene oxide—state-of-the-art encroachment toward polymer nanocompositing. *Polymer-Plastics Techn. Mater.* **2024**, *63*, 872. [[CrossRef](#)]
21. Abidi, S.S.A.; Murtaza, Q. Synthesis and Characterization of Nano-hydroxyapatite Powder Using Wet Chemical Precipitation Reaction. *J. Mater. Sci. Technol.* **2014**, *30*, 307–310. [[CrossRef](#)]
22. Tang, B.; Yun, X.; Xiong, Z.; Wang, X. Formation of Graphene Oxide Nanoscrolls in Organic Solvents: Toward Scalable Device Fabrication. *ACS Appl. Nano Mater.* **2018**, *1*, 686–697. [[CrossRef](#)]
23. Ajala, O.; Werther, C.; Nikaeen, P.; Singh, R.P.; Depan, D. Influence of graphene nanoscrolls on the crystallization behavior and nano-mechanical properties of polylactic acid. *Polym. Adv. Technol.* **2019**, *30*, 1825–1835. [[CrossRef](#)]
24. Wang, P.; Yu, T.; Lv, Q.; Li, S.; Ma, X.; Yang, G.; Xu, D.; Liu, X.; Wang, G.; Chen, Z.; et al. Fabrication of hydroxyapatite/hydrophilic graphene composites and their modulation to cell behavior toward bone reconstruction engineering. *Colloids Surf. B Biointerfaces* **2019**, *173*, 512–520. [[CrossRef](#)]
25. Neelgund, G.M.; Oki, A.; Luo, Z. In situ deposition of hydroxyapatite on graphene nanosheets. *Mater. Res. Bull.* **2013**, *48*, 175–179. [[CrossRef](#)]
26. Chandrasekar, A.; Sagadevan, S.; Dakshnamoorthy, A. Synthesis and characterization of nano-hydroxyapatite (n-HAP) using the wet chemical technique. *Int. J. Phys. Sci.* **2013**, *8*, 1639–1645.

27. Trakoolwannachai, V.; Kheolamai, P.; Ummartyotin, S. Characterization of hydroxyapatite from eggshell waste and polycaprolactone (PCL) composite for scaffold material. *Compos. Part B Eng.* **2019**, *173*, 106974. [[CrossRef](#)]
28. Verma, N.; Zafar, S.; Talha, M. Influence of nano-hydroxyapatite on mechanical behavior of microwave processed polycaprolactone composite foams. *Mater. Res. Express* **2019**, *6*, 085336. [[CrossRef](#)]
29. Ashraf, M.A.; Peng, W.; Zare, Y.; Rhee, K.Y. Effects of Size and Aggregation/Agglomeration of Nanoparticles on the Interfacial/Interphase Properties and Tensile Strength of Polymer Nanocomposites. *Nanoscale Res. Lett.* **2018**, *13*, 214. [[CrossRef](#)]

**Disclaimer/Publisher's Note:** The statements, opinions and data contained in all publications are solely those of the individual author(s) and contributor(s) and not of MDPI and/or the editor(s). MDPI and/or the editor(s) disclaim responsibility for any injury to people or property resulting from any ideas, methods, instructions or products referred to in the content.